

On the origin of the common reactivity and properties of heme peroxidases: a DFT study

Daniel R. Ramos (<http://orcid.org/0000-0002-7963-9119>),^{*,1,2} Paul G. Furtmüller (<http://orcid.org/0000-0002-1199-2469>),³ Christian Obinger (<http://orcid.org/0000-0002-7133-3430>),³ Ángeles Peña-Gallego (<https://orcid.org/0000-0002-6898-8305>),² Ignacio Pérez-Juste (<https://orcid.org/0000-0003-3756-3563>),² J. Arturo Santaballa (<http://orcid.org/0000-0003-0593-8009>)^{*,1}

¹ Chemical Reactivity & Photoreactivity Group (React!), Department of Chemistry, CICA & Faculty of Sciences, Universidade da Coruña, Campus da Zapateira s/n, E-15071 A Coruña, Spain.

² Departamento de Química Física, Universidade de Vigo, Campus Universitario Lagoas-Marcosende, E-36310 Vigo, Spain.

³ Institute of Biochemistry, Department of Chemistry, University of Natural Resources and Life Sciences, Muthgasse 18, A-1190 Vienna, Austria.

*Corresponding authors: Daniel R. Ramos and J. Arturo Santaballa. (React!), Department of Chemistry, CICA & Faculty of Sciences, Universidade da Coruña, Campus da Zapateira s/n, E-15071 A Coruña, Spain. E-mails: daniel.ramos@udc.es, arturo.santaballa@udc.es

Abstract

Electronic structure calculations have been carried out to examine the effect of protonation and water molecules on the heme group of peroxidases in different redox (ferric, ferrous, compounds I and II) and spin states. Shared geometries, spectroscopic properties at Soret region, and thermodynamics of peroxidases are discussed. B3LYP and M06-2X density functionals with different basis sets were employed on a common molecular model of the active site (Fe-centred porphine and proximal imidazole). Computed Gibbs free energies indicate that the corresponding aquo complexes are not thermodynamically stable, supporting the five-coordinate Fe(III) centre in native ferric peroxidases, with a water molecule located at a non-bonding distance. Protonation of the ferryl oxygen of compound II is discussed in terms of thermodynamics, Fe–O bond distances, and redox properties. It is demonstrated that this protonation is necessary to account for the experimental data and computed Gibbs free energies that reveal pK_a values of compound II about 8.5 – 9.0. Computation suggests that the origin of the general oxidative properties of peroxidase species, as well as their reactivity towards water and protons and Soret spectral properties, mostly resides on the iron porphyrin and its proximal ligand histidine.

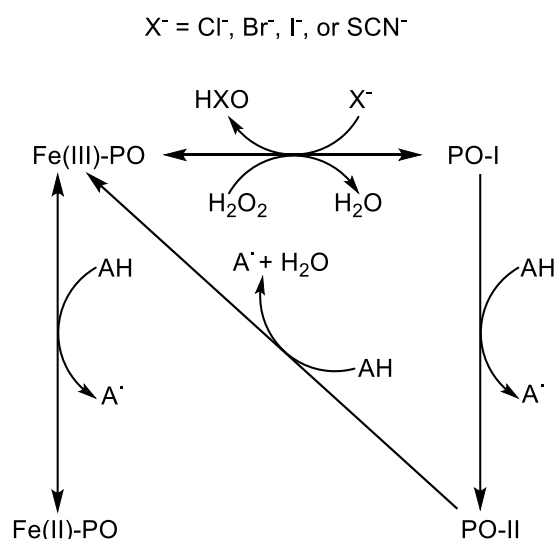
Keywords

Peroxidase; density functional calculations; compound I; compound II; ferryl oxygen; reduction potential.

1. Introduction

Heme-containing proteins and enzymes are ubiquitous and catalyse many different reactions including electron transfer, oxygen binding, oxidations, oxygenations, etc [1,2]. Heme peroxidases use heme *b* or posttranslationally modified heme to catalyse the hydrogen peroxide-mediated one- and two-electron oxidation of a myriad of molecules including aromatic molecules, cations, anions, or even proteins. Four heme peroxidase superfamilies arose independently during evolution, which differ in overall fold, active site architecture (e.g. histidine or cysteine as proximal ligand), and enzymatic activities [3].

Peroxidases operate in a complex multistep mechanism including several redox intermediates (Scheme 1), which were studied by various experimental [4,5] and computational [6-8] means. In general, native ferric peroxidase (Fe(III)-PO) uses H₂O₂, or other oxidants, to generate a ferryl (Fe(IV)=O) π -cation radical complex called compound I (PO-I), having incorporated one oxygen atom derived from heterolytic cleavage of hydrogen peroxide [9]. This species can be one-electron reduced to compound II (PO-II), which also contains a ferryl group, while reversible reduction of the ferric protein yields the ferrous species (Fe(II)-PO).



Scheme 1. Interconversion between peroxidase species: Fe(III)-PO, ferric state; Fe(II)-PO, ferrous state; PO-I, compound I; PO-II, compound II.

Most experimental studies on the electronic structure and reactivity of peroxidases were carried out under neutral or basic conditions, whereas less attention was paid to acidic pH values despite the fact that the pH optimum of many peroxidase activities is below pH 7. For example, chloride oxidation by human myeloperoxidase (MPO) is significantly more efficient at pH 5 compared to pH 7 [5,10-13]. Crystal structures of many peroxidases show the presence of a discrete water in an axial position to the heme iron in the distal cavity [9]. Under acidic pH conditions the occurrence of H₂O and H⁺ rather than HO⁻ at the distal heme cavity has to be taken into account.

Protons are directly involved in peroxidase reactivity (Scheme 1) and, as a consequence, protonation of the ferryl centre has been a central issue to justify the different Fe–O bond distances measured with X-ray diffraction structural analysis for compounds I and II [14]. On the other hand, oxo-ferryl stretching frequencies obtained with resonance Raman spectroscopy (RR) suggest that both compounds exhibit a similar short Fe–O distance [15,16], indicative of unprotonated ferryl oxygen [17]. Extended X-ray absorption fine structure (EXAFS) experiments also support unprotonated compound II [18]. However, iron photoreduction may occur upon X-ray radiation or even due to laser excitation, leading to some uncertainty about the metal oxidation state in those measurements [19-21]. Thus, some inconsistencies have been found, for example long Fe–O distance measured by X-ray diffraction in compound I of cytochrome *c* peroxidase (CCP) [22], or short [18] and long [23] Fe–O distances obtained with EXAFS for horseradish peroxidase (HRP) compound II. Protonation of the ferryl oxygen has been observed for chloroperoxidase (CPO, a heme enzyme with proximal thiolate) compound II by RR [24] and EXAFS [25], whereas myoglobin compound II seems to be unprotonated even at pH 3.9 according to RR and EXAFS measurements [26]. The neutron structures of the ferric and compound I states from CCP [27] and compound II from ascorbate peroxidase (APX) [28] are available, and show the presence of a Fe(IV)-OH group in compound II.

Peroxidases share many properties and have similar molecular structures at the active site. However, the only common part of all these enzymes, at least for three superfamilies, is the Fe-centred porphine ring coordinated to a proximal imidazole. The proximal histidine may display different positions, which influence imidazole rotation, and it is surrounded by rather dissimilar environments that affect its charge distribution. Other examples of variability include the mode of interaction of heme substituents with the protein matrix or even the posttranslational modification of those substituents as shown in representatives of the peroxidase-cyclooxygenase superfamily [2]. On the other hand, conserved amino acids are found on the distal side, such as the catalytic pairs histidine/arginine or aspartate/arginine, but their positions vary with respect to heme and also with respect to their interactions with the distal protein matrix. Therefore, it seems that the prevalent behaviour of these enzymes actually arises from just a quite small part of their active site, while the specific performance of a particular peroxidase results from the remaining part of the active site and its environment. A full mechanistic understanding of peroxidases needs, in addition to study the impact of the protein, the knowledge of the underlying chemistry of all relevant redox intermediates, which cannot be provided by experimental means only. For unravelling mechanistic details in (bio)chemistry [29], electronic structure calculations can be very helpful as they can focus on just a small part of the system.

The aim of this work is the correct description of some common general features of peroxidases, such as protonation state and pK_a values, stability of aqueous complexes, UV-vis spectra or reduction potentials, by means of electronic structure calculations using a suitable common molecular model together with a computational level that yields reliable data at low computational cost. To this end geometric, electronic, and thermodynamic parameters of a reduced model of the active site of native

ferric peroxidase, ferrous peroxidase, peroxidase compound I and compound II, and their aquo and protonated complexes have been calculated. Obtained computational data are compared with experimental data to examine the suitability of both the molecular model and the method of calculation, and to successfully elucidate protonation states and interactions with distal water molecules. Furthermore, this work offers a simple methodology to obtain additional information on different heme peroxidases that cannot be gathered by experimental techniques, and it also emerges as an adequate starting point for further computational research on these enzymes in general, or for the analysis of more specific properties of single peroxidases by *ad hoc* modification of the molecular model employed to account for the particular structure and specific reactivity.

2. Computational details

2.1 Models

Computational studies on heme proteins have used several molecular models of the active site, ranging from very few atoms surrounding the heme metal centre to others concerning the whole protein [30]. Some research was performed using full porphyrin and axial imidazole, which was the choice in this study [17]. Peripheral substituents and their interaction with the protein can affect heme configuration; accordingly, a usual approach in electronic structure calculations dealing with heme porphyrins is to use X-ray structures to consider such effects rather than including the interaction partners in heavy geometry optimizations [31]. However, questions arose as to whether crystal arrangements are the same as in solution; in fact, some differences between solution (NMR) and crystal geometries of cytochrome *c* have been observed [32].

Besides the described general peroxidase behaviour, peroxidases of the four superfamilies [3] exhibit diverse enzymatic activities at different optimum conditions. The origin of these differences is related to variations in the multistep reaction mechanisms, triggered by the protein environment. The use of a specific experimental structure would lead to a particular property, and not to the desired general peroxidase behaviour, which is the aim of this study. On the other hand, the use of geometry optimization on isolated porphyrins may lead to electronic ground states different from those seen in proteins [33]. Compromising previous evidence, in this work the active site was modelled by using Fe-centred porphine, *i.e.* the porphyrin ring without any side chains, and an imidazole ring coordinated to the metal in an axial position, mimicking the proximal histidine (Fig. 1). The latter is found in three out of four heme peroxidases superfamilies [3]. This arrangement was selected on account of studies showing that the axial imidazole substantially enhances the binding energy of ligands in contrast to vinyl and propionate side chains [33-35], which are modified in the peroxidase-cyclooxygenase superfamily [3]. The distal sixth coordination site is either vacant in ferric and ferrous states of peroxidases or eventually occupied by a water molecule, while an oxygen atom plays the role as sixth ligand in the case of the ferryl species compound I and compound II. According to crystallographic studies, water molecules (or related species) are closer to the heme iron or ferryl oxygen atoms than any other amino acid residue. In

addition, protonation reactions might occur. The present computational study considers all possible scenarios (even the untenable ferric and ferrous species with protonated iron) to perform an exhaustive analysis. It should be taken into account that this reduced model of the active site ignores the influence of the protein on heme stabilization, but this effect cancels out when comparing different species.

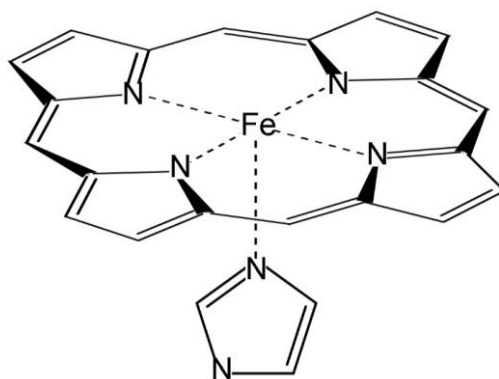


Figure 1. Molecular arrangement employed to model the active site of peroxidases.

2.2 Methods

The suitability of different DFT functionals for correct calculation of a Fe-centred porphyrin ring coordinated to an imidazole group, *i.e.* the same model used in this work, has been studied by comparison of these methods with the results obtained with high-level CCSD(T) calculations with large basis sets for several model iron compounds [36]. All studied functionals showed a good performance in geometry optimization with respect to crystal structures. Also, hybrid DFT functionals yielded reasonably accurate relative energies of the different spin states at a lower computational cost. Additionally, some results obtained for bond dissociation energies of iron ligands suggest that B3LYP describes bonding to oxygen-containing ligands more accurately than other functionals [36]. On the other hand, the M06-2X functional shows a better performance to calculate weak interactions [37], as those found between heme and some other functional groups present in the distal cavity, like water molecules. Electron and spin densities for iron porphyrins were also calculated with both DFT and coupled cluster methods [38-40]. The good agreement between obtained results corroborates the validity of the DFT computations for the comparison of relative energies and evaluation of the stability of the different states of the considered systems.

Thus, DFT-based calculations were done using two hybrid functionals: the Becke's three-parameter method [41] with the correlation functional of Lee, Yang and Parr, incorporating local and non-local terms [42,43] (B3LYP), and the meta exchange-correlation variation of the M06 functional of Zhao and Truhlar that includes double non-local exchange, M06-2X [44]. Split-valence People basis sets [45] 6-31G(d,p), 6-311G(2d,2p) and 6-311++G(2d,2p), and correlation-consistent Dunning basis sets [46] cc-pVDZ, cc-pVTZ, Aug-cc-pVTZ and cc-pVQZ were employed for all atoms but for Fe, where an effective core potential [47] was used to substitute its core electrons with the LANL2DZ basis set.

All calculations were performed with the polarized continuum model (PCM) [48] to take into account the influence of water molecules contained in the distal heme pocket. Water has a more essential effect on the four species studied than bulk protein, as the solvent interacts more closely with the iron atom and the oxo-ferryl group, and these interactions must differ notably between redox intermediates. The cavity used for PCM calculations was built employing atomic radii of the United Atom Topological Model (UA0). Gaussian default values were selected for solvent (water) and for all other parameters of spheres definition.

Geometry optimization reveals essential to adequately reproduce the structures and, as a result, their thermodynamics. Therefore, all considered species were geometrically optimized at B3LYP/cc-pVDZ. Harmonic frequencies were calculated to obtain zero-point energies and thermal corrections to enthalpies and Gibbs free energies at 298.15 K. Full geometry optimization was carried out at low- and high-spin for Fe(III)-PO, PO-I, and PO-II. The d^6 Fe(II) atom can exhibit three spin states: $S = 0$ (low-spin), $S = 1$ (intermediate-spin), and $S = 2$ (high-spin). Therefore, in the case of ferrous species data from these states are calculated in this work. In the remainder of the paper total spin will be referred to either as S (Σs) or as the corresponding multiplicity. Some relevant structures were also fully optimized and their frequencies calculated with both functionals and the seven basis sets selected.

Excitation energies were calculated with the time-dependent DFT (TD-DFT) approach considering the lowest 50 singlet excited states. UV-vis convoluted spectra were extracted from Gaussian output files using the GaussView program [49] by using Gaussian distributions with a peak half-width of 2500 cm^{-1} . This combination was successfully applied to obtain UV-vis spectra for similar chemical systems [50], and yields adequate maximum heights of the Soret band for comparison with experimental values. Position of the iron atom with respect to heme plane was worked out as depicted in Figure 2. Best-fitting plane was obtained from the four pyrrole nitrogen atoms (pyrrole plane), and distance to Fe (Fe-pp) was calculated. Relevant bond orders in all considered species were calculated using the natural bond orbital (NBO) analysis of Weinhold *et al* [51-53]. All calculations were performed with Gaussian 16 [54].

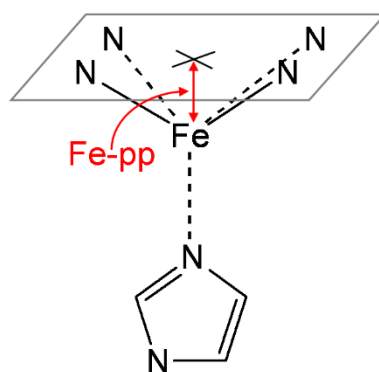
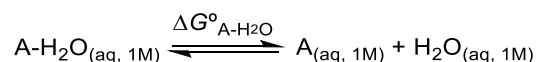


Figure 2. Iron out-of-plane distance (Fe-pp), described as the distance between iron atom and the plane defined by the four pyrrole nitrogen atoms.

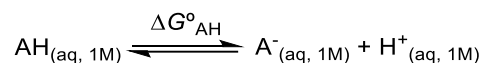
2.3 Calculation of thermodynamic parameters

The dissociation equilibrium of water complexes *in vacuo* is expressed by the following equation:



All computational values involving solvation were corrected as for the standard state in aqueous solution. Water concentration is usually taken as 55.5 M, but this is not the case within the distal cavity of peroxidases, where only some discrete molecules have been detected; therefore, also 1 M concentration has been considered for water.

Thermodynamics of protonation processes are generally reported by the corresponding $\text{p}K_a$ value. Its computational estimation requires the calculation of the optimized geometry and corresponding Gibbs free energy of the protonated and unprotonated forms of the ionizable groups under study, according to the following acid-base equilibrium:



The protonated form, denoted AH, has a net positive charge one unit higher than the unprotonated form, A^- . The expression utilized for the absolute $\text{p}K_a$ calculation is given by:

$$\text{p}K_a = \Delta G^\circ_{\text{AH}} / 2.303RT$$

Again, solvation values must be corrected to consider the transformation of concentration units in going from the gas phase to the aqueous phase (atm to $\text{mol}\cdot\text{dm}^{-3}$). Published thermodynamic parameters were employed for proton in the gas phase [55] and aqueous solution [56,57].

The absolute one-electron reduction potential of any species A can be obtained through the corresponding reduction reaction:



Note that the standard state for e^- is the gas phase, its Gibbs free energy was obtained from reference [58]. The absolute reduction potential is calculated as:

$$E^\circ = - \frac{\Delta G^\circ_{A/A^-}}{nF}$$

where n is the number of electrons generated in the half-reaction and F is the Faraday constant. Reduction potentials are usually reported as relative to the standard hydrogen electrode (SHE) with an absolute reduction potential $E^\circ = 4.44$ V at 298.15 K [59], although slightly different values are obtained if other references for the absolute potential of SHE are employed [60].

The computational estimation of the thermodynamics of protonation processes reported as $\text{p}K_a$ values and the reduction potentials can be calculated with the direct methods mentioned above or with the isodesmic method, where results are improved by balancing the reactions with similar systems used as reference (at the same computational level) [61]. Therefore, phenol deprotonation ($\text{p}K_a = 9.99$) [62] was selected as the complementary reaction for the determination of all isodesmic $\text{p}K_a$ values [63]. An

advantage of this procedure is that the use of uncertain thermodynamic data for the proton is not required [64]. On the other hand, the average reduction potential of compound I to ferric species measured for some native peroxidases, without considering enzymes belonging to the peroxidase cyclooxygenase superfamily, ($E^\circ = 0.926$ V) [65] was the reference employed to correct the potential [66] of the other reduction processes. Similarly, the corresponding value for the compound I to compound II reduction reaction ($E^\circ = 0.977$ V) [65] was then used to calculate the compound I to ferric state reduction potential.

3. Results and discussion

All structures, fully optimized at the most stable spin state, are shown in Figure 3. Ferric native enzyme (Fe(III)-PO) and ferrous species (Fe(II)-PO), as well as aquo complex of the latter, are depicted at high-spin state. The protonated ferrous state, Fe(II)-PO-H, shows an intermediate-spin state. All other species correspond to low-spin. Relevant geometrical parameters and bond orders are collected in Table S1 at the supplementary information. Representative corresponding geometrical data empirically measured for HRP [67,68], CCP [14,22,27], APX [14,28,69], LPO (lactoperoxidase) [70], and MPO [71] are also gathered in Table S2, and are employed as experimental reference values along the manuscript for comparison. In this model, imidazole is not linked to the protein and, therefore, exhibits free rotation around its axial position, while this movement would be more constrained if the proximal His and whole peptide chain were considered. According to previous computational studies this rotation only accounts for a few kJ mol^{-1} [72], so that calculated orientation of this imidazole is disregarded in the discussion. Significant net Mulliken charges [73] calculated at the B3LYP/cc-pVDZ level are shown in Table S3.

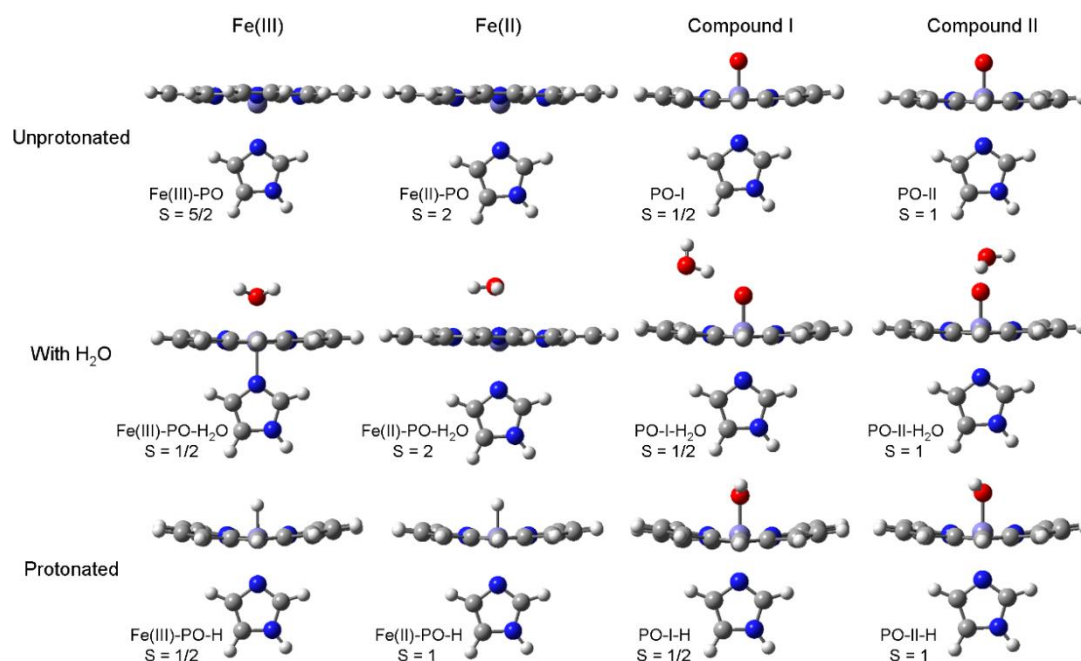


Figure 3. Structures optimized at the B3LYP/cc-pVDZ computational level and at the most stable feasible spin state for Fe(III) native peroxidase, ferrous species, compound I, and compound II, either unprotonated or with a bonded H₂O discrete molecule or protonated at a distal axial position.

Relative Gibbs free energy values are collected in Table 1. The parent unprotonated species with the experimental most stable spin were used as reference, their absolute free energy values, as well as other employed data, are compiled in Table S4.

Table 1. Gibbs free energy obtained with B3LYP/cc-pVDZ ($T = 298.15$ K) for all the compounds under study optimized at low and high spin (and intermediate spin for ferrous species). Most stable species of each unprotonated compound was taken as reference. Relative data of protonated and aquo complexes were worked out with respect to separate parent unprotonated species plus H^+ or H_2O as appropriate.

Species	Spin	$\Delta G^\circ / \text{kJ mol}^{-1}$
Fe(III)-PO	1/2	49.73
	5/2	0.00
Fe(III)-PO-H ₂ O	1/2	-12.44
	5/2	0.86
Fe(III)-PO-H	1/2	269.21
	5/2	307.07
Fe(II)-PO	0	46.38
	1	59.96
	2	0.00
Fe(II)-PO-H ₂ O	0	25.66
	1	63.38
	2	5.13
Fe(II)-PO-H	0	231.01
	1	179.50
	2	221.61
PO-I	1/2	0.00
	5/2	49.61
PO-I-H ₂ O	1/2	9.95
	5/2	59.44
PO-I-H	1/2	24.06
	5/2	86.53
PO-II	1	0.00
	2	56.93
PO-II-H ₂ O	1	4.53
	2	62.60
PO-II-H	1	-48.66
	2	-9.19

3.1 Unprotonated species

Ferric and ferrous intermediates

B3LYP computations yield a high-spin Fe(III)-PO 50 kJ·mol⁻¹ more stable than the doublet. A similar difference (46 kJ mol⁻¹) was obtained between high- and low-spin species in the case of Fe(II)-PO, while the triplet is 60 kJ mol⁻¹ above the resting state. Bare Fe(III)-PO and Fe(II)-PO share similar geometry, even closer when considering equivalent spin states. Slightly out-of-plane Fe atom in the proximal direction is observed, more evident in the case of high-spin species, while heme planarity remains despite the shift of the metal. Metal bonding to imidazole is clearly tighter for low-spin species, as indicated by both the Fe–N_i (imidazole N) distances and bond orders. Distances between the heme iron and pyrrole nitrogens, Fe–N_p (pyrrole N), are nearly equal for Fe(III)-PO and Fe(II)-PO, with variations of only *ca.* 0.02 Å. Computed values for both high-spin species adequately fit in the empirical ranges observed (except for the two representatives of the peroxidase-cyclooxygenase superfamily, namely LPO and MPO), but the outer position of Fe with respect to heme plane is more pronounced in the calculations, probably due to the lack of distal interactions in the model. Higher positive charge (approx. 0.3 a.u.) is observed on Fe(III) atom with respect to Fe(II). Additionally, *ca.* 0.6 a.u. more negative values were obtained for the porphine ring in the case of Fe(II)-PO, accounting for the one-electron reduction process in going from ferric to ferrous species, and the fact that the formation of this species should involve the gain of a proton at the heme moiety.

Compound I and compound II

Calculations yielded an appreciably more stable low-spin in the case of hexacoordinate-Fe compounds PO-I and PO-II (~50 kJ mol⁻¹), which also exhibit a very similar geometry. The iron atom is hexacoordinate, forming a strong bond with ferryl oxygen (O_{Fe}), characterized by a short distance (≤ 1.63 Å) and bond orders higher than one (~1.4). This results in a somewhat longer Fe–N_i bond with respect to Fe(III)-PO, especially in the case of PO-II. Similar Fe–O_{Fe} distances have been measured for CCP compound I both by X-ray and neutron diffraction crystallography, whereas other peroxidases show a slightly longer bond. This bond distribution involves an out-of-plane metal centre displaced towards the distal direction, which is strongly influenced by the spin state. For both compounds, O_{Fe} exhibits a charge between –0.30 and –0.35 a.u., mostly counterweighed by less negative charge in the porphine ring and slightly higher positive charge on Fe, with respect to ferric and ferrous species. Compound I in most heme peroxidases contains a porphyrin π-cation radical, and analogously a positive charge on this ring is obtained in the case of PO-I, only observed in the protonated form of other oxidation states. In the real system, the porphyrin charge must be more positive considering the effect of heme side chains and interactions with adjacent protein. Upon addition of ferryl oxygen to the model, heme planarity is mostly conserved, although minor saddle-type conformation is observed.

3.2 Aquo complexes

Ferric and ferrous intermediates

Addition of one water molecule causes minor molecular reorganization, primarily a displacement of Fe into porphyrin plane, more evident in the case of the ferric species, which results in some lengthening of the Fe–N_i bond, while heme planarity is retained. The obtained geometries of the aquo complexes of ferric and ferrous intermediates are, therefore, more similar than observed with bare species. A very weak bond is formed between the metal and water oxygen (O_w). The associated Wiberg bond indices [74] are characteristic of hydrogen bonding. Fe–O_w distance calculated for the ferric species is shorter than for most of the reference peroxidases, although APX shows a water molecule even closer to the metal. On the other hand, calculations on the aquo-ferrous complex yield the water molecule situated at a further distance compared with experimental data. These complexes were produced by photoreduction of a ferryl species (compound I), and in this process ferryl oxygen converts into water. Structures obtained by direct reduction of ferric native enzymes could be different, at least with regard to the location of this water molecule. The water molecule is axially placed in all optimized geometries, as revealed by a ~180° angle with respect to N_i, observed in crystallographic structures as well, and shows a net positive charge, indicating that charge transfer takes place between porphine ring and water molecule.

The presence of water at the sixth coordination site stabilizes preferentially low- (and, to a minor extent, intermediate-) spin species, but the effect is different depending on the enzymatic species considered. In the case of Fe(III)-PO-H₂O, the low-spin species is much more stabilized, arising from the effective hexacoordination of the metal atom (Fe–O_w bond order = 0.39, almost twice the high-spin value, and more charge is transferred in this case), due to the more adequate electronic occupancy of iron *d*-orbitals for distal binding. Thus, the single species with *S* = 5/2 is preferred, but the ordering is inverted when a discrete water solvation is considered. The water molecule linked to Fe(II)-PO-H₂O presents an interaction with Fe that becomes stronger for decreasing spin values. It modifies consequently the relative stability of spin states but the Gibbs free energy preference is not altered. Water addition also causes a charge reallocation in these two species, the positive charge on Fe decreases as some electronic density is transferred from H₂O; this effect is more evident in the ferric complex, where obtained Fe–O_w bond orders are higher (Tables S1 & S3).

The obtained dissociation energies of water complexes, $\Delta G^{\circ}_{A-H_2O}(aq)$, at preferred spin states are collected in Table 2. The negative value calculated for Fe(II)-PO-H₂O indicates that this complex is unstable: bonding to ferrous centre is weak and $\Delta G^{\circ}_{A-H_2O}(aq) = -5.12 \text{ kJ mol}^{-1}$. In the case of Fe(III)-PO-H₂O the stabilization caused by Fe–O interaction is also weak but enough to compensate the loss of aqueous PCM solvation energy, and the formation of the complex (at B3LYP/cc-pVDZ level) is favourable. However, hydrogen bonding of the water molecule to either other water molecules or available adequate residues in the distal cavity (typically 5 to 30 kJ mol⁻¹ per H-bond) could rule out the possibility of formation of thermodynamically favourable aquo-complexes. However, calculations with

other basis sets (Table S5) yield negative $\Delta G^{\circ}_{\text{A-H}_2\text{O}}(\text{aq})$ values for this species, the more negative the bigger the basis employed. Furthermore, results obtained employing the M06-2X functional yield more positive numbers, which also decrease to very low values when increasing the basis set. Contrary to B3LYP results, structures calculated with M06-2X are more stable at high spin, and, therefore, Fe–O_w distances are longer and show weaker interactions. To summarise, results with B3LYP plus (at least) triple- ζ basis sets and with M06-2X with any basis set, which are consistent with empirical data, show that ferric iron of native peroxidases is pentacoordinated while a water molecule is situated at a distal position but at a long non-bonding distance.

Table 2. Gibbs free energy values in kJ mol^{-1} for the dissociation equilibrium of the different considered aquo complexes ($\Delta G^{\circ}_{\text{A-H}_2\text{O}}(\text{aq})$), and $\text{p}K_{\text{a}}$ values for corresponding protonation processes, calculated directly ($\text{p}K_{\text{a}}^1$) and with the isodesmic method ($\text{p}K_{\text{a}}^2$). All data calculated by B3LYP/cc-pVDZ ($T = 298.15 \text{ K}$). The most favourable spin multiplicities were used; first value under spin columns refers to unprotonated species, second number to the aquo complex or protonated compound.

Species	Spin	$\Delta G^{\circ}_{\text{A-H}_2\text{O}}(\text{aq})$	Spin	$\text{p}K_{\text{a}}^1$	$\text{p}K_{\text{a}}^2$
Fe(III)-PO	5/2 – 1/2	12.44	5/2 – 1/2	–47.2	–60.7
Fe(II)-PO	2 – 2	–5.12	2 – 1	–31.4	–45.0
PO-I	1/2 – 1/2	–9.95	1/2 – 1/2	–4.2	–17.7
PO-II	1 – 1	–4.53	1 – 1	8.5	–5.0

Compound I and compound II

Contrary to previous heme-aquo complexes, addition of H-bonded water to PO-I and PO-II causes only a minor polarization on both the water molecule and the heme moiety. Some negative charge is transferred to the ferryl oxygen from the metalloporphyrin, whereas significant net charge transfer from water is not observed, but this molecule undergoes a certain charge polarization as well. This discrete water molecule does not lie at the distal axis. Connecting H forms a $\sim 120^{\circ}$ angle with respect to Fe, typical of an sp^2 hybridised orbital, which corresponds to the electronic configuration of a double bonded oxygen atom (Fe=O) [75]. Wiberg bond analysis yields a very low $\text{O}_{\text{Fe}}\text{–H}$ value, which indicates a weak H-bond, accompanied by a slight change in the length and strength (a weakening) of the Fe–O_{Fe} ferryl bond and an opposite effect on the Fe–N_i bond. Still, calculated forces seem stronger than in peroxidase crystals, where the angles are also different, as water molecules in the distal cavity generally lie at a quite further distance from O_{Fe} and are stabilized by other surrounding interactions.

The dissociation energies are consequently affected, with $\Delta G^{\circ}_{\text{A-H}_2\text{O}}(\text{aq})$ values ranging from -5 to -10 kJ mol^{-1} , but the spin preference is not modified. The effect on oxygen charge, and on length and strength of the Fe–O_{Fe} double bond is quite similar for both ferryl species. The calculated Fe–O_{Fe} distance is adequate in the case of PO-I-H₂O (1.634 \AA vs experimental $1.635 - 1.743 \text{ \AA}$), while the short elongation

observed for this bond in PO-II-H₂O (also 1.634 Å) does not seem enough to reproduce the longer Fe–O_{Fe} distance determined by crystallography for compound II (1.830 – 1.879 Å). The interaction is weak and the dissociation process is favourable. However, the position of the water molecule in this case (distance from the metal to water oxygen > 3.8 Å) could allow a less stressed cooperative interaction of H₂O with both the ferryl group and other suitable residues placed above heme in the distal cavity, taking advantage of the stabilization by extensive H-bonding. Therefore, water molecules, present in the distal cavity, may easily interact with compounds I and II while they keep away from the metal centre of ferric and ferrous species, as this sole interaction reveals thermodynamically unfavourable. Furthermore, hydrogen bonding cannot solely explain the differences observed between compound I and compound II.

3.3 Protonated species

The effect of protonation on geometry, charge and spectral properties is more relevant than in the previous results obtained with water complexes. Thus, when a proton is added to the model, electronic density is transferred from the heme moiety to H⁺, while H₂O only caused certain bond polarization and the net charge transferred was much lower. This leads to some structural modification and subsequent thermodynamical changes.

Ferric and ferrous intermediates

Protonation does not produce any significant effect on heme structure. However, a shift is observed in the Fe position, which becomes closer to the heme pyrrole plane. The bond to imidazole nitrogen weakens in low-spin species and the opposite effect is observed in high-spin structures. Formation of a bond between H⁺ and the iron atom of the ferric and ferrous species (Fe(III)-PO-H and Fe(II)-PO-H) seems a very unfavourable process, as it involves a cation with no electron density available for donation acting as sixth ligand of Fe³⁺ / Fe²⁺. However, when linked to the metal centre, the calculated charge on this atom approaches to zero for any spin state, but the high-spin ferric complex, while effective Fe–H bonding is observed (bond orders > 0.5). This electronic density has been fully transferred from the porphine ring. Proton addition to ferrous and ferric species produces some distortion on heme planarity. The shorter the Fe–H bond, the more evident the effect, causing a saddle-shape conformation of heme (displacement of two opposite meso carbon atoms of methine bridges towards distal side while the other two move in the proximal direction) that is coupled with asymmetric Fe–N_p linkages.

Protonated Fe(III)-PO-H presents a more stable low-spin state, which develops from the hexacoordinate Fe(III) atom, while *S* = 1 species is more favoured for Fe(II)-PO-H. Furthermore, protonation involves a very significant destabilization effect on the ferric and ferrous species. Therefore, both Fe(III)-PO and Fe(II)-PO present very negative p*K*_a values, either calculated directly or with the isodesmic method (Table 2). This can be explained by the high positive charge on the iron atom plus the partial desolvation of H⁺ in the distal cavity. Therefore, these two species do not accept a proton coordinated to iron even at high acidic aqueous conditions. Besides, extreme acid media lead to inactivation and denaturalization

of the enzymes, which would occur ahead of any iron protonation.

According to the above, the protonation processes experimentally observed for ferric and ferrous species must be assigned to other ionizable groups in the heme or its close vicinity. Chiavarino *et al.* studied computationally the relative energies of ferrous heme protonated at different sites [76]. A much more favourable protonated species (61.9 kJ mol^{-1}) was obtained at the β carbon atom of a vinyl group, and this position was assigned to the gained proton. Anyway, the observed stabilization relative to the protonated iron species would only lead to an increase of $\sim 10 \text{ pK}_a$ units, still insufficient to account for the proton addition upon Fe(II)-PO formation.

Compound I and compound II

Of great significance is the evident lengthening coupled with bond order decrease observed for Fe–O_{Fe} in the case of protonated compound I and compound II. The distance calculated for PO-I-H is longer than all experimental values, whereas the Fe–O_{Fe} bond distance obtained for PO-II-H (1.807 \AA) is in good agreement with all four compound II structures used as reference ($1.830 - 1.879 \text{ \AA}$). A concerted strengthening of the Fe–N_i interaction both in terms of distance and bond order is produced as the metal undergoes a slight in-plane shift (PO-II-H at spin $S = 2$ reveals anomalous, but it also shows a weaker Fe–O_{Fe} bond than the other structures). This effect is not clearly observed in the experimental data. Besides, heme planarity becomes somewhat distorted, attaining saddle-like conformation, more apparent at the lowest spin states. The proton effectively binds O_{Fe} (bond order ~ 0.75) and charge transference takes place from the heme but, in this case, keeping some proton character, *i.e.* computations yield a remaining positive charge *ca.* 0.2 a.u. on this atom. Further polarization is also observed upon protonation. Thus, O_{Fe} increases its negative charge very little ($< 0.1 \text{ a.u.}$) while the positive charge mostly accumulates on the porphine ring. The weakening of the Fe–O_{Fe} bond results in a different hybridization of O_{Fe} atom, approaching to sp^3 , revealed by the lower Fe–O_{Fe}–H angle. However, the opposite behaviour was observed for protonated APX compound II (142°), perhaps related to other distal interactions, although this proton does not form a linear H-bond to any other neighbouring atom, but the proximity of a water molecule could be responsible for some steric distortion.

Changes in structure and charge distribution are rather similar for the protonation of these two species (but the abnormal high-spin PO-II-H), and also parallel to the effect observed upon water addition, although to a higher extent. Still, no change in the relative stability of the different spin states is observed, and low-spin species are again preferred. The effective O_{Fe}–H linkage is the responsible of the more favourable free energy values obtained for these protonated species. It must be noted that the stabilization upon protonation is always higher for PO-II-H, and that the protonation of compound II is a spontaneous process (49 kJ mol^{-1}).

The pK_a obtained for compound I with both methods is negative (Table 2), which means that this species is never protonated. Still, PO-I-H is much more stable than the ferric and ferrous structures protonated at the metal centre. The protonated form of compound II presents a geometry very similar to PO-I-H but with lower Gibbs free energy with respect to the unprotonated species, resulting in a positive pK_a value

when computed directly, but again negative when the calculation is performed with respect to phenol. Results obtained with other basis sets (Table S6) follow the same trend: negative values for PO-I-H, and around 8 for PO-II-H, which become mostly negative when calculated with the isodesmic method. However, this profile changes drastically when the M06-2X functional is employed. In this case, PO-I-H pK_a data range from 8 to 18 (direct method), decreasing to values close to 0 when calculated with respect to phenol deprotonation. These amended results also rule out the possibility of compound I protonation. On the other hand, pK_a values in the range 21 – 23 are obtained for PO-II-H, which reduce to 8 – 15 after the isodesmic correction. In both cases, this indicates that this compound is protonated at the normal enzyme function. These numbers may correspond to the pK_a range found in the literature for compound II of HRP A (6.9) [15,77], other HRP isozymes (8.5) [15], or other peroxidases (~9) [78,79]. As commented above, protonation on ferryl oxygen of compound II is still controversial. Often, this process has been ascribed to the distal histidine, despite the pK_a corresponding to the deprotonation of free histidine imidazole is only 6.0, much lower than the value observed in peroxidases. Besides, the neutral form of imidazole should be favoured in the interior of a protein. It does not seem reasonable that the effect of a ferryl oxygen situated at 3.6 – 3.8 Å from imidazole N atom [14,67] could cause such an increase (2.5 to 3 pK_a units). However, the presence of this neighbouring distal imidazole and some water molecules could lead to a more moderate variation of the ferryl oxygen pK_a (*ca.* ± 1 unit). Thus, even considering that this effect is neglected in the molecular model used and the error of the computational method, we can assume that the pK_a value around 8.5 – 9.0 measured for compound II could correspond to the ionization of protonated ferryl group. Recently, another study obtained pK_a values for a basic compound II ferryl oxygen of porphyrins [80] similar to the model used in this paper but lacking the proximal imidazole. The effect of this coordination bond is quite relevant as other hemoproteins with different proximal ligands show rather dissimilar activities and, presumably, the acidity of this proton also diverges. Additionally, the nature of ferryl group interactions within distal cavity should be different for PO-I and PO-II-H. We could suggest a different protonation state of distal His, as the interaction with unprotonated or protonated ferryl group must also have a different effect on this imidazole, but it does not conform to neutron diffraction results, where this group appears protonated in both CCP compound I and APX compound II. Although it should be taken into account that there is not a porphyrin π -cation radical in the former but a proximal tryptophan radical [81]. Considering that compound I exhibits a very low pK_a value and that the pK_a obtained for compound II could be equivalent to the experimentally measured value around 8.5 – 9.0 or even higher, the ferryl oxygen of these two species must be unprotonated and protonated, respectively, as observed with neutron diffraction crystallography [27,28], except for all the enzymes belonging to three heme peroxidases superfamilies.

3.4 Spectral properties

Despite the particular structure of the different proteins, the position and intensity of the Soret band for the different redox intermediates are quite conserved for the whole peroxidase family. Differences arise from the specific protein environment surrounding heme moiety and, in particular, from the covalent linkages between heme and protein. Soret band of ferric peroxidases is located around 405 nm with a molar absorption coefficient *ca.* 100000 $\text{cm}^{-1}\cdot\text{M}^{-1}$. In the case of compound I, the intensity is reduced to approximately 50% at the same wavelength. On the contrary, compound II exhibits a band of similar intensity to that of ferric species ($\sim 90000 \text{ cm}^{-1}\cdot\text{M}^{-1}$) but shifted to the 420 nm region. Ferrous species presents a more red-shifted Soret band (440 nm) with $\epsilon = 85000 \text{ cm}^{-1}\cdot\text{M}^{-1}$. All these data are average values of experimental results found in the literature for several peroxidases after excluding outliers, namely MPO, which holds three covalent bonds to the protein via two ester bonds and one sulfonium linkage, and nonplanar porphyrin group. As a consequence MPO exhibits a particularly red-shifted band scheme [50,82].

Convolutated calculated spectra at the UV region, showing the Soret band area, of the four here studied unprotonated species at the most stable spin state are collected in Figure 4A (more spectral data are presented as supplementary material, Table S7). Absorption maxima exhibit a net blue shift of 30 – 50 nm relative to the experimental data, along with an adequate intensity profile. This blue shift has been previously reported and is due to the known low performance of the employed TD-DFT functional in the description of excitation energies [83,84], as well as the absence of the porphyrin side chains in the molecular model [50]. As the origin of this deviation is the same, the absolute error obtained in the calculations can be expected to be similar for all considered species. Thus, relative wavelengths would reproduce experimental spectral shifts more accurately.

A minor red shift on the computed Soret spectra was obtained when a water molecule is considered (Figure 4B), coupled with some reduction of the extinction coefficient, except for Fe(III)-PO-H₂O, where it increases slightly. The predicted relative wavelength of PO-I is 5 nm higher than that of Fe(III)-PO (368 nm), but very similar to its aqueous complex (372 nm), and PO-I relative extinction coefficient is too high ($58000 \text{ cm}^{-1} \text{ M}^{-1}$), although lower than in both ferric species ($70000 - 72000 \text{ cm}^{-1} \text{ M}^{-1}$). The spectrum of the aquo complex of compound I, PO-I-H₂O, has less intensity ($52000 \text{ cm}^{-1} \text{ M}^{-1}$ at 375 nm) but still much higher than half the ferric peaks. Red shifts of 11 – 16 nm and 15 – 20 nm were obtained for compound II and ferrous complexes, respectively, with respect to ferric species. This behaviour is consistent with observed experimental red shifts, although to a lesser extent.

Computed protonated enzymatic complexes (Figure 4C) yield UV-vis absorption profiles at the Soret band region with very low intensity with respect to both unprotonated species and the experimental spectral properties. Only PO-II-H shows a significant peak ($57000 \text{ cm}^{-1} \text{ M}^{-1}$ at 370 nm), which is not adequately red shifted; this could be related to the lack of some interactions with surrounding groups, missing in the computational model employed, and would need further analysis.

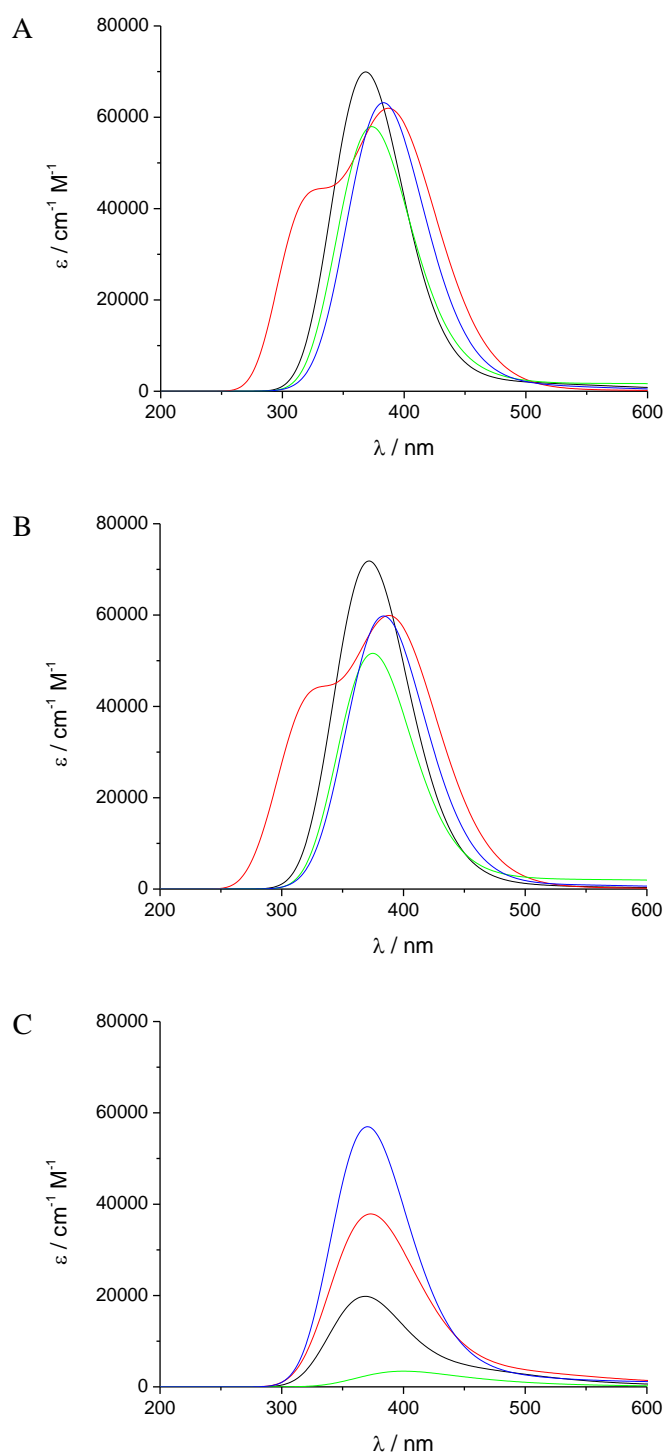


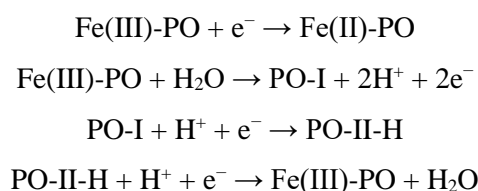
Figure 4. UV-vis spectra (Soret region) obtained by TD-DFT calculations with the B3LYP/cc-pVDZ computational level at the most stable spin multiplicity for (A) unprotonated Fe(III)-PO (—), Fe(II)-PO (—), PO-I (—), and PO-II (—); (B) corresponding aquo complexes; and (C) protonated species.

3.5 Redox properties

Peroxidases participate in one- and two-electron oxidation processes. The native ferric state is oxidized to compound I, which is either directly reduced by two-electron donors (*e.g.* halides) to the ferric state or by one-electron donors to compound II and subsequently to the resting state, which can also be reduced to ferrous state (Scheme 1). Both oxidized intermediates exhibit a higher oxidation capacity compared to ferric and ferrous species. Redox properties of all these intermediates have been measured for different peroxidases. The standard reduction potential of the redox couple Fe(III)/Fe(II) typically ranges between -120 and -310 mV [65]. Human myeloperoxidase is unique in having a globin-like reduction potential at $+5$ mV [85] due to an electron withdrawing covalent sulfonium ion bond between the prosthetic group and a methionine.

The redox intermediate with the highest oxidation capacity is compound I. In heme *b* peroxidases the reduction potential E° values of the couple compound I/ferric state and compound I/compound II were reported to be in the range $750 - 950$ mV and $900 - 1150$ mV, respectively [65]. By contrast, in representatives of the peroxidase-cyclooxygenase superfamily, which typically have posttranslationally modified and covalently linked heme, the E° values of the redox couples compound I/compound II and compound I/ferric state are more positive, namely $1000 - 1150$ mV and $1150 - 1350$ nm, respectively [86,87]. Reduction potentials for the redox couple compound II/ferric state were reported to be in the range of $750 - 950$ mV for heme *b* peroxidases and $950 - 1050$ mV for members of the peroxidase-cyclooxygenase superfamily [3].

Reduction of ferric species and all individual redox processes involved in the peroxidase cycle were calculated theoretically, including oxidation of native peroxidase to yield compound I, reduction of compound I to compound II and, finally, reduction of compound II to the ferric state:



The respective standard reduction potentials relative to SHE, E° , for all these individual redox steps have been calculated (Table 4). Half reactions were modified to account for the protonated and unprotonated forms of compound II, while only unprotonated ferrous species was considered.

Table 4. Standard reduction potential (E°) values in mV relative to SHE calculated with direct and isodesmic methods, at B3LYP/cc-pVDZ and M06-2X/cc-pVTZ computational levels ($T = 298.15$ K). The most favourable spin multiplicities were used (as specified in parentheses).

	Reduction half-reaction					
	Fe(III)-PO/Fe(II)-PO	PO-I/Fe(III)-PO	PO-I/PO-II	PO-I/PO-II-H	PO-II/Fe(III)-PO	PO-II-H/Fe(III)-PO
	(5/2 – 2)	(1/2 – 5/2)	(1/2 – 1)	(1/2 – 1)	(1 – 5/2)	(1 – 5/2)
Direct method						
B3LYP/cc-pVDZ	377	1066	741	1245	1391	886
M06-2X/cc-pVTZ	662	2358	1120	2380	3596	2336
Isodesmic method						
B3LYP/cc-pVDZ	237	798	601	1105	1251	747
M06-2X/cc-pVTZ	-770	955	-312	948	2164	904

Obtained reduction potential values calculated with the direct method are very dependent on the basis set and, particularly, on the functional employed (Tables 4 and S8). Some of the obtained numbers differ considerably from the experimental ranges, but it can still be noticed that the overall redox profile resembles the experimental one only when protonated compound II is considered. On the other hand, isodesmic method results allow a better discussion. Reduction of PO-I to Fe(III)-PO yields E° values between 798 and 1069 mV with B3LYP, and somewhat lower with M06-2X (621 to 989). In both cases, reduction potentials increase with larger basis sets, so that, although all the values seem reasonable, the results obtained with M06-2X plus the best basis sets (triple- ζ at least) are very close to or within the experimental peroxidase range. However, in the case of the B3LYP functional, more adequate results are obtained with the lowest basis sets. Calculation of the reduction potential of the couple compound I/compound II yielded unsatisfactory results when the latter was unprotonated. On the other hand, the values calculated with PO-II-H range 834 – 1105 mV (B3LYP) and 914 – 1282 mV (M06-2X). In this case, the highest values were obtained with double- ζ basis sets and, again, the data that better mirror the experimental values were calculated with lesser and larger basis sets, for B3LYP and M06-2X, respectively. Similarly, E° of the redox couple compound II/ferric state was too high when calculated with unprotonated PO-II (> 1250 mV), and much more adequate data are obtained with PO-II-H, again suggesting the presence of protonated compound II. As in the formation of compound I, the results increase with the basis set and they are closer to the experimental values with worse sets at B3LYP (747 – 918 mV) and with better ones at M06-2X (834 – 938 mV). Finally, the values calculated for the reduction potential of the couple Fe(III)-PO/Fe(II)-PO with B3LYP (-373 to 237 mV) are more suitable than those of M06-2X (-698 to -1133 mV), which are significantly more negative compared to the experimental values. However, assuming that the protonated ferrous species, Fe(II)-PO-H* (protonated on a position other than ferrous centre), is more stable than the unprotonated Fe(II)-PO, more positive reduction potential should be obtained, which would be closer to experimental values. These data

indicate that the origin of the redox properties of the different peroxidase intermediates mostly lies on the metalloporphyrin ring together with proximal imidazole.

3.6 Adequacy of the computational molecular model and method

It was our clear aim to check the performance of a molecular model comprised of ferriporphine and a proximal imidazole, the only fully common part for three out of four heme peroxidase superfamilies. Distal catalytic residues were not incorporated in the model as their chemistry and distance from the metal centre significantly vary in peroxidases from the four superfamilies. Also, heme side chains are modified in members of the peroxidase-cyclooxygenase superfamily, and the position and environment of proximal histidine greatly differs among peroxidases.

Very slight geometrical changes have been obtained among the different computational methods employed, but some relevant differences have been found in the thermodynamical parameters studied. The changes in optimized geometries are negligible for the purpose of this study and, more important, they do not affect the conclusions. The most important divergence in thermodynamical results occurs between the two functionals used. So, much more positive values have been obtained for $\Delta G^\circ_{A-H_2O}(aq)$ of Fe(III)-PO-H₂O, and a more favoured high-spin aqueous complex, with M06-2X. However, when combined with large basis sets, the results discard the possibility of a distal water molecule bonded to ferric iron, but agree with this axial water molecule situated at a non-bonding distance. The direct calculation of pK_as and standard reduction potentials yields defective values, which can be highly improved with the isodesmic method. To this end, the use of one of the half-reactions from the peroxidase cycle (two-electron reduction of PO-I to Fe(III)-PO) to correct the potential values of the other steps was quite successful. Consistent redox profiles were obtained with all computational levels, always provided that compound II is protonated; but the data calculated with M06-2X plus cc-pVTZ (or higher) fit better the experimental results. Furthermore, too low pK_a values were computed with B3LYP for PO-II-H, which do not support the protonation of this species at neutral pH, and notably higher with M06-2X. Therefore, thermodynamical values calculated with the B3LYP functional are in general worse compared to those obtained with M06-2X, in particular when they are employed together with at least triple- ζ basis sets.

We do not claim that this reduced model of the active site of peroxidases could reproduce the detailed behaviour of a particular enzyme as it does not include the effect of heme side chains, heme-protein linkages, and full protein environment. However, it does include the most important common structural features of their active site, and reproduces the general behaviour and common characteristics. Despite their different protein structure, peroxidases share a variety of physicochemical properties (similar spectroscopic and redox characteristics, reactivity, active site geometry, etc.), and the specific features of any particular peroxidase must be attributed to slight variations of external influences on the core of the active site. Therefore, this simple molecular arrangement coupled with PCM solvation at the B3LYP/cc-pVDZ computational level revealed adequate for a general elucidation of the geometry of

the studied structures, while M06-2X/cc-pVTZ is necessary to reproduce satisfactorily several common thermodynamical properties of peroxidases. The latter method can be also successfully employed in computational studies with other similar systems.

4. Conclusions

Electronic structure calculations have been carried out to examine the effect of protonation and hydrogen-bonded water molecules on peroxidase species at a distal axial position. This is the first comprehensive computational study on ferric and ferrous states, as well as compound I and compound II of peroxidases, by using a minimal molecular model common to all these enzymes and at different spin multiplicities. The use of this simple molecular arrangement together with B3LYP full geometry optimization and frequency calculations, with unspecific surrounding interactions simulated by means of PCM water solvation, and employing LANL2DZ for Fe and cc-PVDZ for other atoms, allowed a correct prediction of electronic ground states as well as a reasonable description of the UV spectra at the Soret region. Besides, obtained geometries show a good correlation with experimental structures. To calculate adequate thermodynamic parameters, such as $\Delta G^\circ_{A-H_2O}(aq)$ values, pK_a values, and reduction potentials (E°), the M06-2X/cc-pVTZ computational level is required.

Gibbs free energy data revealed that distal bonding of a water molecule at the sixth position of ferric peroxidases is thermodynamically unstable, thus supporting five-coordinate metal atom of these enzymes with a water molecule axially situated but at non-bonding distance from the Fe(III) centre. Furthermore, unfavourable interaction with discrete water molecules was also obtained for other studied species since aquo complexes are less stable than separate solvated corresponding heme model and H_2O ($\Delta G^\circ_{A-H_2O}(aq) < 0$). Similarly, axial proton addition at the distal side does not occur under physiological conditions, as revealed by the low pK_a values, except for a more favourable ferryl oxygen protonation in the case of compound II. This proton is responsible for the longer Fe–O_{Fe} distance observed with X-ray diffraction experiments. Besides, a protonated ferryl oxygen of compound II is necessary to justify the redox potential obtained for processes involving this species. Current computational results indicate that this feature must be common to all peroxidases and not only APX, which was already established by neutron diffraction studies, and the estimated pK_a could correspond to the value around 8.5 – 9.0 experimentally measured for compound II, the first time a value has been proposed.

In summary, although specific characteristics of particular enzymes arise from the environment and heme-peptide linkages, obtained results tell about the adequacy of both the molecular model for characterization of most common peroxidase features and the employed methodologies, which can be extended to other similar systems, with no experimental data available. Observed agreement between computation and experiment suggests that the origin of the general oxidative profile of peroxidase species, as well as their reactivity towards water and protons and Soret spectral properties, mostly resides on just the iron porphyrin and the proximal histidine moiety.

Supplementary Information

Relevant geometrical parameters, bond orders, Mulliken atomic charges, and spectral properties calculated with B3LYP/cc-pVDZ; absolute energies used as reference values; experimental values for comparison; and dissociation equilibrium values of Fe(III)-PO-H₂O, pK_as of compounds I and II, and standard reduction potentials obtained by B3LYP and M06-2X functionals with different basis sets.

Abbreviations

HRP, horseradish peroxidase; MPO, myeloperoxidase; CCP, cytochrome *c* peroxidase; CPO, chloroperoxidase; APX, ascorbate peroxidase; LPO, lactoperoxidase; SHE, standard hydrogen electrode; Fe(III)-PO, native ferric peroxidase; Fe(II)-PO, ferrous peroxidase; PO-I, peroxidase compound I; PO-II, peroxidase compound II; Fe(III)-PO-H₂O, Fe(II)-PO-H₂O, PO-I-H₂O, and PO-II-H₂O, aquo complexes of previous species, respectively; Fe(III)-PO-H, Fe(II)-PO-H, PO-I-H, and PO-II-H, protonated forms, respectively.

Acknowledgments

This work was funded by the Spanish *Ministerio de Ciencia e Innovación* (project PID2021-127898OB-I00), and the regional government *Xunta de Galicia* through projects GPC ED431B 2020/52 and GRC ED431C 2019/24. D. R. Ramos acknowledges the Spanish *Ministerio de Universidades* and *Universidade da Coruña* for a *Margarita Salas* postdoctoral fellowship. Thanks are also given to the *Centro de Supercomputación de Galicia* (CESGA) for computing facilities.

Conflicts of Interest

The authors declare no conflict of interest.

Author Contributions

Conceptualization, D.R.R. and J.A.S.; Methodology, D.R.R., A.P.G. and I.P.J.; Formal Analysis, all the authors; Investigation, D.R.R.; Writing – Original Draft Preparation, D.R.R.; Writing – Review & Editing, all the authors; Funding Acquisition, J.A.S., A.P.G. and I.P.J.

References

1. Ortiz de Montellano, P.R. *Cytochrome P-450: structure, mechanism, and biochemistry*; Plenum Press: New York, 1986.
2. Everse, J.; Everse, K.E.; Grisham, M.B. *Peroxidases in chemistry and biology*; CRC Press: Boca Raton, FL, 1991.
3. Zámocký, M.; Hofbauer, S.; Schaffner, I.; Gasselhuber, B.; Nicolussi, A.; Soudi, M.; Pirker, K.F.; Furtmüller, P.G.; Obinger, C. Independent evolution of four heme peroxidase

- superfamilies. *Arch. Biochem. Biophys.* **2015**, *574*, 108-119, doi:<https://doi.org/10.1016/j.abb.2014.12.025>.
4. Poulos, T.L.; Kraut, J. The stereochemistry of peroxidase catalysis. *J. Biol. Chem.* **1980**, *255*, 8199-8205, doi:[https://doi.org/10.1016/S0021-9258\(19\)70630-9](https://doi.org/10.1016/S0021-9258(19)70630-9).
 5. Ramos, D.R.; García, M.V.; Canle L., M.; Santaballa, J.A.; Furtmüller, P.G.; Obinger, C. Myeloperoxidase-catalyzed taurine chlorination: initial versus equilibrium rate. *Arch. Biochem. Biophys.* **2007**, *466*, 221-233, doi:<https://doi.org/10.1016/j.abb.2007.07.024>.
 6. Harris, D.L.; Loew, G.H. Identification of putative peroxide intermediates of peroxidases by electronic structure and spectra calculations. *J. Am. Chem. Soc.* **1996**, *118*, 10588-10594, doi:<https://doi.org/10.1021/ja9617247>.
 7. Loew, G.; Dupuis, M. Structure of a model transient peroxide intermediate of peroxidases by ab initio methods. *J. Am. Chem. Soc.* **1996**, *118*, 10584-10587, doi:<https://doi.org/10.1021/ja961723e>.
 8. Barea, G.; Maseras, F.; Lledós, A. Theoretical assessment on the viability of possible intermediates in the reaction mechanism of catalase and peroxidase models. *J. Mol. Struct.-Theochem* **2003**, *632*, 323-333, doi:[https://doi.org/10.1016/S0166-1280\(03\)00309-9](https://doi.org/10.1016/S0166-1280(03)00309-9).
 9. Dunford, H.B. *Heme peroxidases*; John Wiley & Sons, Inc.: New York, 1999.
 10. Spalteholtz, H.; Panasenko, O.M.; Arnhold, J. Formation of reactive halide species by myeloperoxidase and eosinophil peroxidase. *Arch. Biochem. Biophys.* **2006**, *445*, 225-234, doi:<https://doi.org/10.1016/j.abb.2005.06.025>.
 11. Vlasova, I.I.; Arnhold, J.; Osipov, A.N.; Panasenko, O.M. pH-dependent regulation of myeloperoxidase activity. *Biochem., Moscow* **2006**, *71*, 667-677, doi:<https://doi.org/10.1134/S0006297906060113>.
 12. Ramos, D.R.; García, M.V.; Canle L., M.; Santaballa, J.A.; Furtmüller, P.G.; Obinger, C. Myeloperoxidase-catalyzed chlorination: The quest for the active species. *J. Inorg. Biochem.* **2008**, *102*, 1300-1311, doi:<https://doi.org/10.1016/j.jinorgbio.2008.01.003>.
 13. Furtmüller, P.G.; Burner, U.; Obinger, C. Reaction of myeloperoxidase compound I with chloride, bromide, iodide, and thiocyanate. *Biochemistry* **1998**, *37*, 17923-17930, doi:<https://doi.org/10.1021/bi9818772>.
 14. Gumiero, A.; Metcalfe, C.L.; Pearson, A.R.; Raven, E.L.; Moody, P.C.E. Nature of the ferryl heme in compounds I and II. *J. Biol. Chem.* **2011**, *286*, 1260-1268, doi:<https://doi.org/10.1074/jbc.M110.183483>.
 15. Sitter, A.J.; Reczek, C.M.; Terner, J. Heme-linked ionization of horseradish peroxidase compound II monitored by the resonance Raman Fe(IV)=O stretching vibration. *J. Biol. Chem.* **1985**, *260*, 7515-7522, doi:[https://doi.org/10.1016/S0021-9258\(17\)39637-0](https://doi.org/10.1016/S0021-9258(17)39637-0).

16. Kincaid, J.R.; Zheng, Y.; Al-Mustafa, J.; Czarnecki, K. Resonance Raman spectra of native and mesoheme-reconstituted horseradish peroxidase and their catalytic intermediates. *J. Biol. Chem.* **1996**, *271*, 28805-28811, doi:<https://doi.org/10.1074/jbc.271.46.28805>.
17. Green, M.T. Application of Badger's rule to heme and non-heme iron-oxygen bonds: An examination of ferryl protonation states. *J. Am. Chem. Soc.* **2006**, *128*, 1902-1906, doi:<https://doi.org/10.1021/ja054074s>.
18. Penner-Hahn, J.E.; Eble, K.S.; McMurry, T.J.; Renner, M.; Balch, A.L.; Groves, J.T.; Dawson, J.H.; Hodgson, K.O. Structural characterization of horseradish peroxidase using EXAFS spectroscopy. Evidence for Fe = O ligation in compounds I and II. *J. Am. Chem. Soc.* **1986**, *108*, 7819-7825, doi:<https://doi.org/10.1021/ja00284a054>.
19. Hough, M.A.; Antonyuk, S.V.; Strange, R.W.; Eady, R.R.; Hasnain, S.S. Crystallography with Online Optical and X-ray Absorption Spectroscopies Demonstrates an Ordered Mechanism in Copper Nitrite Reductase. *J. Mol. Biol.* **2008**, *378*, 353-361, doi:<https://doi.org/10.1016/j.jmb.2008.01.097>.
20. Hersleth, H.-P.; Andersson, K.K. How different oxidation states of crystalline myoglobin are influenced by X-rays. *BBA-Proteins Proteomics* **2011**, *1814*, 785-796, doi:<https://doi.org/10.1016/j.bbapap.2010.07.019>.
21. Pfanzagl, V.; Beale, J.H.; Michlits, H.; Schmidt, D.; Gabler, T.; Obinger, C.; Djinić-Carugo, K.; Hofbauer, S. X-ray-induced photoreduction of heme metal centers rapidly induces active-site perturbations in a protein-independent manner. *J. Biol. Chem.* **2020**, *295*, 13488-13501, doi:<https://doi.org/10.1074/jbc.RA120.014087>.
22. Bonagura, C.A.; Bhaskar, B.; Shimizu, H.; Li, H.; Sundaramoorthy, M.; McRee, D.E.; Goodin, D.B.; Poulos, T.L. High-resolution crystal structures and spectroscopy of native and compound I cytochrome c peroxidase. *Biochemistry* **2003**, *42*, 5600-5608, doi:<https://doi.org/10.1021/bi034058c>.
23. Chance, B.; Powers, L.; Ching, Y.; Poulos, T.; Schonbaum, G.R.; Yamazaki, I.; Paul, K.G. X-ray absorption studies of intermediates in peroxidase activity. *Arch. Biochem. Biophys.* **1984**, *235*, 596-611, doi:[https://doi.org/10.1016/0003-9861\(84\)90234-0](https://doi.org/10.1016/0003-9861(84)90234-0).
24. Stone, K.L.; Behan, R.K.; Green, M.T. Resonance Raman spectroscopy of chloroperoxidase compound II provides direct evidence for the existence of an iron(IV)-hydroxide. *Proc. Natl. Acad. Sci. U.S.A.* **2006**, *103*, 12307-12310, doi:<https://doi.org/10.1073/pnas.0603159103>.
25. Green, M.T.; Dawson, J.H.; Gray, H.B. Oxoiron(IV) in chloroperoxidase compound II is basic: Implications for P450 chemistry. *Science* **2004**, *304*, 1653-1656, doi:<https://doi.org/10.1126/science.1096897>.
26. Yosca, T.H.; Behan, R.K.; Krest, C.M.; Onderko, E.L.; Langston, M.C.; Green, M.T. Setting an upper limit on the myoglobin iron(IV)hydroxide pK_a: Insight into axial ligand tuning in heme

- protein catalysis. *J. Am. Chem. Soc.* **2014**, *136*, 9124-9131, doi:<https://doi.org/10.1021/ja503588n>.
27. Casadei, C.M.; Gumiero, A.; Metcalfe, C.L.; Murphy, E.J.; Basran, J.; Concilio, M.G.; Teixeira, S.C.M.; Schrader, T.E.; Fielding, A.J.; Ostermann, A.; et al. Neutron cryo-crystallography captures the protonation state of ferryl heme in a peroxidase. *Science* **2014**, *345*, 193-197, doi:<https://doi.org/10.1126/science.1254398>.
28. Kwon, H.; Basran, J.; Casadei, C.M.; Fielding, A.J.; Schrader, T.E.; Ostermann, A.; Devos, J.M.; Aller, P.; Blakeley, M.P.; Moody, P.C.E.; et al. Direct visualization of a Fe(IV)–OH intermediate in a heme enzyme. *Nat. Commun.* **2016**, *7*, 13445, doi:<https://doi.org/10.1038/ncomms13445>.
29. Maskill, H. *The investigation of organic reactions and their mechanisms*; Blackwell publishing: Oxford, 2006.
30. Ramos, M.J.; Fernandes, P.A. Computational enzymatic catalysis. *Acc. Chem. Res.* **2008**, *41*, 689-698, doi:<https://doi.org/10.1021/ar7001045>.
31. Zhang, Y.; Mao, J.; Godbout, N.; Oldfield, E. Mössbauer quadrupole splittings and electronic structure in heme proteins and model systems: A density functional theory investigation. *J. Am. Chem. Soc.* **2002**, *124*, 13921-13930, doi:<https://doi.org/10.1021/ja020298o>.
32. Banci, L.; Bertini, I.; Gray, H.B.; Luchinat, C.; Reddig, T.; Rosato, A.; Turano, P. Solution structure of oxidized horse heart cytochrome c. *Biochemistry* **1997**, *36*, 9867-9877, doi:<https://doi.org/10.1021/bi970724w>.
33. Rovira, C.; Kunc, K.; Hutter, J.; Ballone, P.; Parrinello, M. Equilibrium geometries and electronic structure of iron-porphyrin complexes: A density functional study. *J. Phys. Chem. A* **1997**, *101*, 8914-8925, doi:<https://doi.org/10.1021/jp9722115>.
34. Rovira, C.; Parrinello, M. Factors influencing ligand binding properties of heme models: a first principles study of picket-fence and protoheme complexes. *Chem. Eur. J.* **1999**, *5*, 250-262, doi:[http://dx.doi.org/10.1002/\(SICI\)1521-3765\(19990104\)5:1%3C250::AID-CHEM250%3E3.0.CO;2-C](http://dx.doi.org/10.1002/(SICI)1521-3765(19990104)5:1%3C250::AID-CHEM250%3E3.0.CO;2-C).
35. Rovira, C.; Parrinello, M. Harmonic and anharmonic dynamics of Fe-CO and Fe-O₂ in heme models. *Biophys. J.* **2000**, *78*, 93-100, doi:[https://doi.org/10.1016/S0006-3495\(00\)76575-1](https://doi.org/10.1016/S0006-3495(00)76575-1).
36. Strickland, N.; Harvey, J.N. Spin-forbidden ligand binding to the ferrous-heme group: Ab initio and DFT Studies. *J. Phys. Chem. B* **2007**, *111*, 841-852, doi:<https://doi.org/10.1021/jp064091j>.
37. Zhang, K.; Chen, L.; Geng, D.; Lu, J.; Wu, J. Thermal stability mechanism via energy absorption by chemical bonds bending and stretching in free space and the interlayer reaction of layered molecular structure explosives. *Phys. Chem. Chem. Phys.* **2020**, *22*, 13248-13260, doi:<https://doi.org/10.1039/D0CP01470B>.

38. Johansson, M.P.; Blomberg, M.R.A.; Sundholm, D.; Wikström, M. Change in electron and spin density upon electron transfer to haem. *Biochim. Biophys. Acta* **2002**, *1553*, 183-187, doi:[https://doi.org/10.1016/S0005-2728\(02\)00182-2](https://doi.org/10.1016/S0005-2728(02)00182-2).
39. Johansson, M.P.; Sundholm, D.; Gerfen, G.; Wikström, M. The spin distribution in low-spin iron porphyrins. *J. Am. Chem. Soc.* **2002**, *124*, 11771-11780, doi:<https://doi.org/10.1021/ja026523j>.
40. Johansson, M.P.; Sundholm, D. Spin and charge distribution in iron porphyrin models: a coupled cluster and density-functional study. *J. Chem. Phys.* **2004**, *120*, 3229-3236, doi:<https://doi.org/10.1063/1.1640343>.
41. Becke, A.D. Density-functional thermochemistry. III. The role of exact exchange. *J. Chem. Phys.* **1993**, *98*, 5648-5652, doi:<https://doi.org/10.1063/1.464913>.
42. Lee, C.; Yang, W.; Parr, R.G. Development of the Colle-Salvetti correlation-energy formula into a functional of the electron density. *Phys. Rev. B* **1988**, *37*, 785-789, doi:<https://doi.org/10.1103/PhysRevB.37.785>.
43. Miehlich, B.; Savin, A.; Stoll, H.; Preuss, H. Results obtained with the correlation energy density functionals of Becke and Lee, Yang and Parr. *Chem. Phys. Lett.* **1989**, *157*, 200-206, doi:[https://doi.org/10.1016/0009-2614\(89\)87234-3](https://doi.org/10.1016/0009-2614(89)87234-3).
44. Zhao, Y.; Truhlar, D.G. The M06 suite of density functionals for main group thermochemistry, thermochemical kinetics, noncovalent interactions, excited states, and transition elements: two new functionals and systematic testing of four M06-class functionals and 12 other functionals. *Theor. Chem. Acc.* **2008**, *120*, 215-241, doi:<https://doi.org/10.1007/s00214-007-0310-x>.
45. Ditchfield, R.; Hehre, W.J.; Pople, J.A. Self-consistent molecular-orbital methods. IX. An extended Gaussian-type basis for molecular-orbital studies of organic molecules. *J. Chem. Phys.* **1971**, *54*, 724-728, doi:<https://doi.org/10.1063/1.1674902>.
46. Dunning Jr., T.H. Gaussian basis sets for use in correlated molecular calculations. I. The atoms boron through neon and hydrogen. *J. Chem. Phys.* **1989**, *90*, 1007-1023, doi:<https://doi.org/10.1063/1.456153>.
47. Hay, P.J.; Wadt, W.R. Ab initio effective core potentials for molecular calculations. Potentials for the transition metal atoms Sc to Hg. *J. Chem. Phys.* **1985**, *82*, 270-283, doi:<https://doi.org/10.1063/1.448799>.
48. Tomasi, J.; Persico, M. Molecular interactions in solution: an overview of methods based on continuous distributions of the solvent. *Chem. Rev.* **1994**, *94*, 2027-2094, doi:<https://doi.org/10.1021/cr00031a013>.
49. Dennington, R.D.; Keith, T.A.; Millam, J.M. *GaussView*, Version 6.0.16; Semichem Inc.: Shawnee Mission, KS, 2016.

50. Devarajan, A.; Gaenko, A.V.; Ryde, U. Effect of covalent links on the structure, spectra, and redox properties of myeloperoxidase - A density functional study. *J. Inorg. Biochem.* **2008**, *102*, 1549-1557, doi:<https://doi.org/10.1016/j.jinorgbio.2008.01.031>.
51. Glendening, E.D.; Reed, A.E.; Carpenter, J.E.; Weinhold, F. *NBO Version 3.1*.
52. Carpenter, J.E.; Weinhold, F. Analysis of the geometry of the hydroxymethyl radical by the "different hybrids for different spins" natural bond orbital procedure. *J. Mol. Struct.-Theochem* **1988**, *169*, 41-62, doi:[https://doi.org/10.1016/0166-1280\(88\)80248-3](https://doi.org/10.1016/0166-1280(88)80248-3).
53. Reed, A.E.; Curtiss, L.A.; Weinhold, F. Intermolecular interactions from a natural bond orbital, donor-acceptor viewpoint. *Chem. Rev.* **1988**, *88*, 899-926, doi:<https://doi.org/10.1021/cr00088a005>.
54. Frisch, M.J.; Trucks, G.W.; Schlegel, H.B.; Scuseria, G.E.; Robb, M.A.; Cheeseman, J.R.; Scalmani, G.; Barone, V.; Petersson, G.A.; Nakatsuji, H.; et al. *Gaussian 16 Rev. C.01*, Wallingford, CT, 2016.
55. Bartmess, J.E. Thermodynamics of the electron and the proton. *J. Phys. Chem.* **1994**, *98*, 6420-6424, doi:<https://doi.org/10.1021/j100076a029>.
56. Tissandier, M.D.; Cowen, K.A.; Feng, W.Y.; Gundlach, E.; Cohen, M.H.; Earhart, A.D.; Coe, J.V.; Tuttle Jr., T.R. The proton's absolute aqueous enthalpy and Gibbs free energy of solvation from cluster-ion solvation data. *J. Phys. Chem. A* **1998**, *102*, 7787-7794, doi:<https://doi.org/10.1021/jp982638r>.
57. Topol, I.A.; Tawa, G.J.; Burt, S.K.; Rashin, A.A. On the structure and thermodynamics of solvated monoatomic ions using a hybrid solvation model. *J. Chem. Phys.* **1999**, *111*, 10998-11014, doi:<https://doi.org/10.1063/1.480486>.
58. Ho, J.; Coote, M.L.; Cramer, C.J.; Truhlar, D.G. Organic electrochemistry. In *Theoretical calculation of reduction potentials*, Fifth edition, Revised and expanded ed.; Hammerich, O., Speiser, B., Eds.; CRC Press: Boca Raton, 2015; pp. 229-259.
59. IUPAC. *Compendium of chemical terminology (the "Gold Book")*, 2nd ed.; Blackwell Scientific Publications: Oxford, 1997.
60. Isse, A.A.; Gennaro, A. Absolute potential of the standard hydrogen electrode and the problem of interconversion of potentials in different solvents. *J. Phys. Chem. B* **2010**, *114*, 7894-7899, doi:<https://doi.org/10.1021/jp100402x>.
61. Arumugam, K.; Becker, U. Computational redox potential predictions: Applications to inorganic and organic aqueous complexes, and complexes adsorbed to mineral surfaces. *Minerals* **2014**, *4*, 345-387, doi:<https://doi.org/10.3390/min4020345>.
62. Haynes, W.M., (Ed.) *CRC Handbook of chemistry and physics*. 95th ed.; CRC Press: Boca Raton, FL, 2014-2015.

63. Sastre, S.; Casasnovas, R.; Muñoz, F.; Frau, J. Isodesmic reaction for accurate theoretical pKa calculations of amino acids and peptides. *Phys. Chem. Chem. Phys.* **2016**, *18*, 11202-11212, doi:<https://doi.org/10.1039/C5CP07053H>.
64. Dutra, F.R.; Silva, C.d.S.; Custodio, R. On the accuracy of the direct method to calculate pKa from electronic structure calculations. *J. Phys. Chem. A* **2021**, *125*, 65-73, doi:<https://doi.org/10.1021/acs.jpca.0c08283>.
65. Battistuzzi, G.; Bellei, M.; Bortolotti, C.A.; Sola, M. Redox properties of heme peroxidases. *Arch. Biochem. Biophys.* **2010**, *500*, 21-36, doi:<https://doi.org/10.1016/j.abb.2010.03.002>.
66. Namazian, M.; Norouzi, P.; Ranjbar, R. Prediction of electrode potentials of some quinone derivatives in acetonitrile. *J. Mol. Struct.-Theochem* **2003**, *625*, 235-241, doi:[https://doi.org/10.1016/S0166-1280\(03\)00070-8](https://doi.org/10.1016/S0166-1280(03)00070-8).
67. Berglund, G.I.; Carlsson, G.H.; Smith, A.T.; Szöke, H.; Henriksen, A.; Hajdu, J. The catalytic pathway of horseradish peroxidase at high resolution. *Nature* **2002**, *417*, 463-468, doi:<https://doi.org/10.1038/417463a>.
68. Carlsson, G.H.; Nicholls, P.; Svistunenko, D.; Berglund, G.I.; Hajdu, J. Complexes of horseradish peroxidase with formate, acetate, and carbon monoxide. *Biochemistry* **2005**, *44*, 635-642, doi:<https://doi.org/10.1021/BI0483211>.
69. Sharp, K.H.; Mewies, M.; Moody, P.C.E.; Raven, E.L. Crystal structure of the ascorbate peroxidase-ascorbate complex. *Nat. Struct. Mol. Biol.* **2003**, *10*, 303-307, doi:<https://doi.org/10.1038/NSB913>.
70. Singh, A.K.; Singh, N.; Sharma, S.; Singh, S.B.; Kaur, P.; Bhushan, A.; Srinivasan, A.; Singh, T.P. Crystal structure of lactoperoxidase at 2.4 Å resolution. *J. Mol. Biol.* **2008**, *376*, 1060-1075, doi:<https://doi.org/10.1016/j.jmb.2007.12.012>.
71. Fiedler, T.J.; Davey, C.A.; Fenna, R.E. X-ray crystal structure and characterization of halide-binding sites of human myeloperoxidase at 1.8 Å resolution. *J. Biol. Chem.* **2000**, *275*, 11964-11971, doi:<https://doi.org/10.1074/JBC.275.16.11964>.
72. Galstyan, A.S.; Zarić, S.D.; Knapp, E.W. Computational studies on imidazole heme conformations. *J. Biol. Inorg. Chem.* **2005**, *10*, 343-354, doi:<https://doi.org/10.1007/s00775-005-0642-8>.
73. Mulliken, R.S. Electronic population analysis on LCAO-MO molecular wave functions. I. *J. Chem. Phys.* **1955**, *23*, 1833-1840, doi:<https://doi.org/10.1063/1.1740588>.
74. Wiberg, K.B. Application of the pople-santry-segal CNDO method to the cyclopropylcarbinyl and cyclobutyl cation and to bicyclobutane. *Tetrahedron* **1968**, *24*, 1083-1096, doi:[https://doi.org/10.1016/0040-4020\(68\)88057-3](https://doi.org/10.1016/0040-4020(68)88057-3).
75. Murray-Rust, P.; Glusker, J.P. Directional hydrogen bonding to sp²- and sp³-hybridized oxygen atoms and its relevance to ligand-macromolecule interactions. *J. Am. Chem. Soc.* **1984**, *106*, 1018-1025, doi:<https://doi.org/10.1021/ja00316a034>.

76. Chiavarino, B.; Crestoni, M.E.; Fornarini, S.; Rovira, C. Protonated heme. *Chem. Eur. J.* **2007**, *13*, 776-785, doi:<https://doi.org/10.1002/chem.200600748>.
77. Hashimoto, S.; Nakajima, R.; Yamazaki, I.; Tatsuno, Y.; Kitagawa, T. Oxygen exchange between the Fe(IV)=O heme and bulk water for the A2 isozyme of horseradish peroxidase. *FEBS Lett.* **1986**, *208*, 305-307, doi:[https://doi.org/10.1016/0014-5793\(86\)81038-9](https://doi.org/10.1016/0014-5793(86)81038-9).
78. Oertling, W.A.; Hoogland, H.; Babcock, G.T.; Wever, R. Identification and properties of an oxoferryl structure in myeloperoxidase compound II. *Biochemistry* **1988**, *27*, 5395-5400, doi:<https://doi.org/10.1021/bi00415a002>.
79. Zhang, H.; Dunford, H.B. Hammett $\rho\sigma$ correlation for reactions of lactoperoxidase compound II with phenols. *Can. J. Chem.* **1993**, *71*, 1990-1994, doi:<https://doi.org/10.1139/v93-248>.
80. Boaz, N.C.; Bell, S.R.; Groves, J.T. Ferryl protonation in oxoiron(IV) porphyrins and its role in oxygen transfer. *J. Am. Chem. Soc.* **2015**, *137*, 2875-2885, doi:<https://doi.org/10.1021/ja508759t>.
81. Sivaraja, M.; Goodin, D.B.; Smith, M.; Hoffman, B.M. Identification by ENDOR of Trp¹⁹¹ as the free-radical site in cytochrome c peroxidase compound ES. *Science* **1989**, *245*, 738-740, doi:<https://doi.org/10.1126/science.2549632>.
82. Fenna, R.E. Myeloperoxidase. In *Handbook of metalloproteins*, Messerschmidt, A., Huber, R., Poulos, T., Wieghardt, K., Eds.; John Wiley & Sons: Chichester, 2001; Volume 1, pp. 211-221.
83. Parac, M.; Grimme, S. A TDDFT study of the lowest excitation energies of polycyclic aromatic hydrocarbons. *Chem. Phys.* **2003**, *292*, 11-21, doi:[https://doi.org/10.1016/S0301-0104\(03\)00250-7](https://doi.org/10.1016/S0301-0104(03)00250-7).
84. Jacquemin, D.; Perpète, E.A.; Scuseria, G.E.; Ciofini, I.; Adamo, C. TD-DFT performance for the visible absorption spectra of organic dyes: conventional versus long-range hybrids. *J. Chem. Theory Comput.* **2008**, *4*, 123-135, doi:<https://doi.org/10.1021/ct700187z>.
85. Battistuzzi, G.; Bellei, M.; Zederbauer, M.; Furtmüller, P.G.; Sola, M.; Obinger, C. Redox thermodynamics of the Fe(III)/Fe(II) couple of human myeloperoxidase in its high-spin and low-spin forms. *Biochemistry* **2006**, *45*, 12750-12755, doi:<https://doi.org/10.1021/bi061647k>.
86. Furtmüller, P.G.; Arnhold, J.; Jantschko, W.; Pichler, H.; Obinger, C. Redox properties of the couples compound I/compound II and compound II/native enzyme of human myeloperoxidase. *Biochem. Biophys. Res. Commun.* **2003**, *301*, 551-557, doi:[https://doi.org/10.1016/S0006-291X\(02\)03075-9](https://doi.org/10.1016/S0006-291X(02)03075-9).
87. Furtmüller, P.G.; Arnhold, J.; Jantschko, W.; Zederbauer, M.; Jakopitsch, C.; Obinger, C. Standard reduction potentials of all couples of the peroxidase cycle of lactoperoxidase. *J. Inorg. Biochem.* **2005**, *99*, 1220-1229, doi:<https://doi.org/10.1016/j.jinorgbio.2005.02.021>.